https://doi.org/10.5194/egusphere-2025-6409
Preprint. Discussion started: 12 January 2026

Optimizing SAR Flood Extent Mapping in Central Chile: The Critical Role of Image Timing

Lester Olivares[1,2] and Gabriel González[2]

[1]Facultad de Ciencias Básicas, Universidad Católica del Maule, Campus San Miguel, Avenida San Miguel 3605, Talca, Chile
[2]National Research Center for Integrated Natural Disaster Management (CIGIDEN), Departamento de Ciencias Geológicas, Universidad Católica del Norte, Avenida Angamos 0610, Antofagasta, Chile

Correspondence: Lester Olivares (leolivares@ucm.cl)

Abstract. This study critically quantifies the temporal uncertainty inherent in flood extent estimation using Sentinel-1 SAR data in the high-relief, flash-flood-prone river systems of Central Chile, following the extreme events of 2023. We applied the iterative Jaccard optimization framework to five sites in the Maule and Mataquito watersheds, identifying the Difference Image Index (DII) as the most robust flood indicator. Our key finding is that the estimation of maximum flood extent is fundamentally limited by the timing of the SAR acquisition. River gauge analysis confirmed a flash-flood regime with an extremely rapid recession rate (river height dropping $\sim 50\%$ within four days of the peak). This rapid drainage means that a delay of 24 - 48 hours results in a severe underestimation of the true flood footprint. While the DII performed best, overall Jaccard scores remained low (≤ 0.6). We conclude that the method's accuracy is primarily constrained by physical limitations - namely, the rapid recession rate and complex topography - rather than the calibration technique itself. Relying solely on the Sentinel-1 revisit cycle is insufficient for operational mapping in such dynamic environments, and we recommend integrating SAR monitoring with hydraulic modeling or high-frequency aerial surveys to accurately interpolate the maximum flood extent.

1 Introduction

Flood detection after extreme hydrometeorological events using satellite remote sensing remains a highly debated topic within the scientific community (Gao, 1996; Fisher et al., 2016; Acharya et al., 2018). Traditionally, multispectral images from missions such as Landsat 5, 7, 8, 9 and Sentinel-2 MSI have been utilized to identify water bodies using methods like Modified Normalized Difference Water Index (MNDWI) and Automated Water Extraction Index (AWEI) (Huang et al., 2018; Feyisa et al., 2014; Hui et al., 2008). These methods, however, rely on passive sensors, which are often hindered by the pervasive cloud cover that typically follows extreme rainfall events.

In recent years, active remote sensors have gained popularity for flood detection due to their ability to penetrate clouds, their higher temporal resolution, and free access (e.g., Moharrami et al., 2021; Tauqeer et al., 2025; Tripathy, 2022). However, the water backscattering intensity signal on a single channel can sometimes be confused with signals from other materials that also exhibit low backscattering intensity, such as dry sand and paved surfaces (Liang and Liu, 2020). Conversely, the backscattering signature of standing water can be modified by surface roughness (e.g., wind-induced waves), potentially increasing the signal and leading to misclassification (Twele et al., 2016). To address these SAR ambiguities, rigorous methodologies have been

https://doi.org/10.5194/egusphere-2025-6409
Preprint. Discussion started: 12 January 2026

developed, including approaches that iteratively optimize the threshold using the Jaccard Index against an optical reference (Hamidi et al., 2023). This robust framework utilizes established SAR indices like the Difference Image Index (DII), the Ratio Index (RI), and the Normalized Difference Flood Index (NDFI). While robust, this methodology has not been rigorously tested in flash-flood-prone, high-relief environments, where the rapid recession rate fundamentally limits the utility of a fixed satellite revisit cycle. This study, therefore, applies this methodology to the topographically diverse Central Chile not only to provide an accurate, locally tuned flood extent estimation, but critically, to quantify the temporal uncertainty introduced by image acquisition timing. However, the unobserved maximum flood extent introduces a critical uncertainty, which can be detrimental for informed hazard planning and decision-making by stakeholders, particularly where complementary approaches, such as hydrodynamic modeling, are scarce or absent.

To address these limitations, the present study establishes a robust framework with three primary objectives. First, the analysis is refined by integrating crucial ancillary geospatial data—namely the Global Surface Water layer and a Digital Elevation Model—to rigorously mitigate false positives associated with permanent water bodies and areas of steep slope, thus ensuring the flood detection focuses on areas most suitable to flooding. Second, we define an optimal, locally-tuned flood detection methodology by iteratively validating three distinct SAR indices (DII, RI, and NDFI) with the nearest-temporal Sentinel-2 MNDWI data, which allows us to quantify the most suitable threshold value for the Chilean Central zone. Finally, we critically quantify the uncertainty in event-based flood mapping by analyzing the mapped extent across multiple Sentinel-1 acquisition dates relative to the local precipitation peak, assessing the influence of image timing on the estimated flood area.

2 Methodology

2.1 Study area and data acquisition

The study focuses on the central zone of Chile (35°S–36°S), a densely populated region characterized by its distinct geomorphology, including the Coastal Cordillera, the Central Depression, and the Main Cordillera. This area was severely impacted by two distinct extreme hydrometeorological events: the June 2023 event (peak precipitation around June 22–24) and the August 2023 event (peak precipitation around August 19–21), as shown in Figure 1. These events were selected for analysis due to the significant human impact they caused (CIGIDEN, 2023) and their characteristic heavy cloud cover, which necessitated the use of Synthetic Aperture Radar (SAR) for flood delineation. To ensure a robust evaluation of the methodological framework across varied topographies, five specific areas of interest were selected within the Mataquito and Maule watersheds (Figure 2). These sites were chosen based on their high vulnerability and their distinct geomorphological positions: one area in the Coastal Cordillera, two at the boundary of the Central Depression and Coastal Cordillera, and two at the boundary of the Main Cordillera and Central Depression. The comparison across these diverse sites allows us to critically assess how flood extent estimation varies, not only temporally but also in response to local terrain complexity.

https://doi.org/10.5194/egusphere-2025-6409
Preprint. Discussion started: 12 January 2026

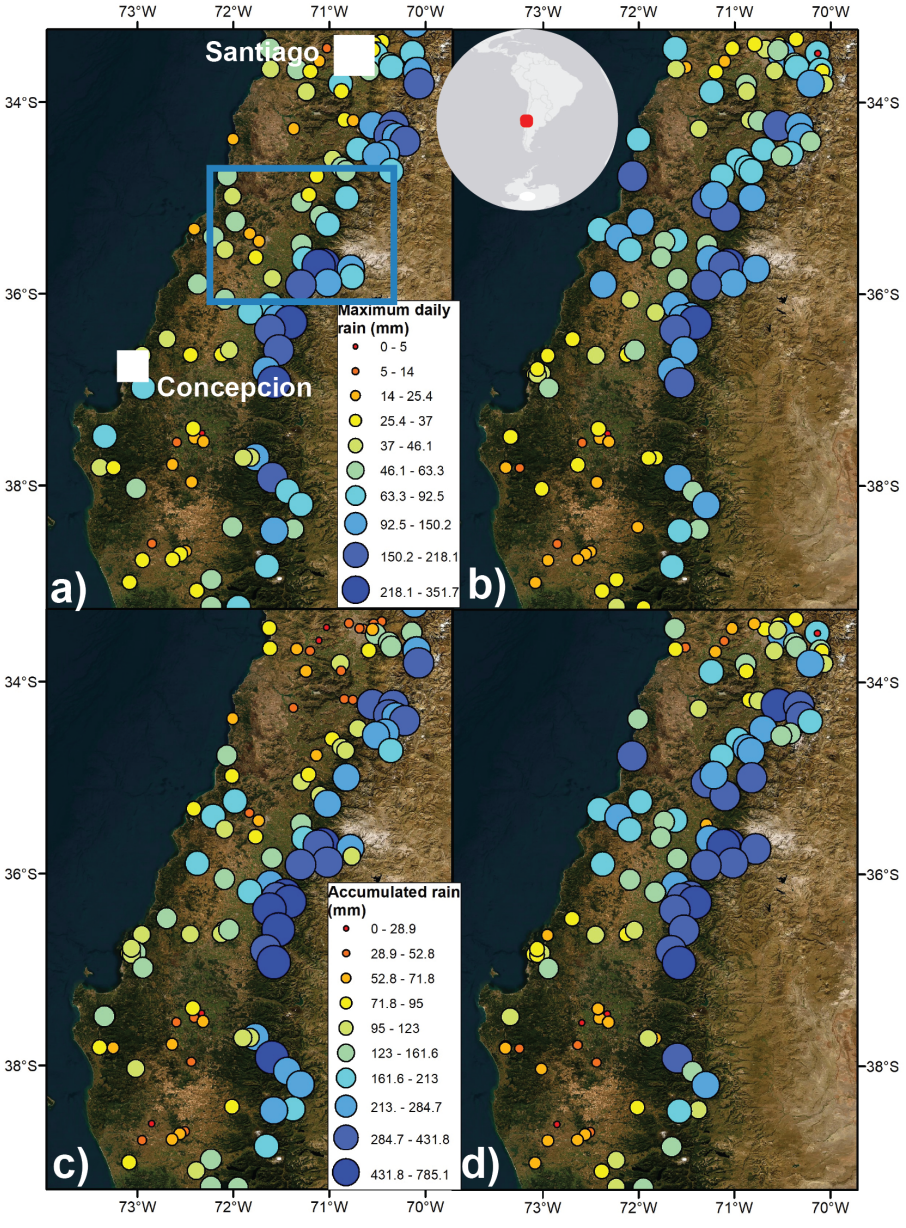

Figure 1. Rain distribution in June and August 2023. a) Maximum daily rainfall during the June event. The blue rectangle indicates the study area shown in Figure 2. b) Maximum daily rainfall during the August event. The data in (a) and (b) are displayed with the same color legend for comparison. c) Accumulated rainfall for the June event. d) Accumulated rainfall for the August event. Note that the data in (c) and (d) are displayed with the same color legend. The dataset used here was downloaded from https://explorador.cr2.cl

https://doi.org/10.5194/egusphere-2025-6409
Preprint. Discussion started: 12 January 2026

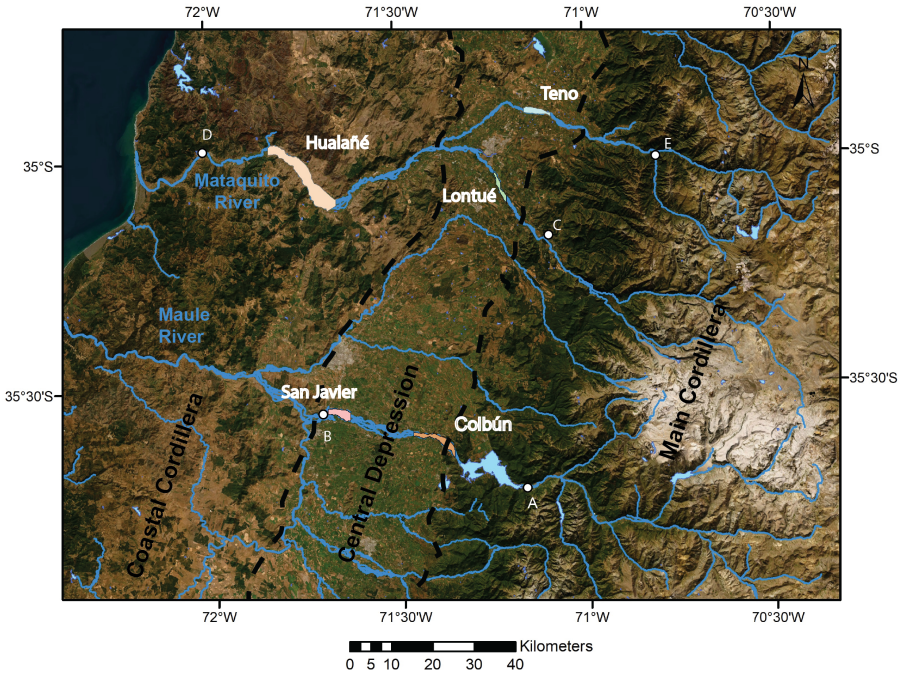

Figure 2. The satellite image displays five analyzed areas, each delineated by a different colored polygon. The blue lines shows the relevant drainage networks. White dots with letters mark the locations of the Dirección General de Aguas (DGA) river gauges. The codes for these gauges are as follows: A = Canal de evacuación C. Pehuenche (07321005-4), B = Río Maule en Longitudinal (07322001-7), C = Estero Upeo en Upeo (07116001-7), D = Río Mataquito en Licantén (07123001-5), and E = Río Claro en los Queñes (07103001-6).

2.2 Data processing and pre-analysis

The entire methodological process, including data acquisition, pre-processing, and index optimization, was implemented using Google Earth Engine (GEE) algorithms in a Google Colab environment.

2.2.1 Hydrometeorological event characterization and river gauge analysis

To characterize the temporal progression of the two extreme events, rainfall evolution was assessed using the GPM IMERG Final Precipitation L3 database in Google Earth Engine (Huffman et al., 2019). Drainage areas connected to the five study sites were calculated using the Hydrology toolbox in ArcGIS 10.2 and the Copernicus 30-meter DEM (European Space Agency, 2024). Given the low spatial resolution ($\sim$ 10 km) but high temporal resolution (3 hours) of the GPM dataset, the average rainfall was aggregated over each calculated drainage area into 24-hour periods. The standard deviation was also calculated for each period. This process allowed for the precise definition of the progression of each rain event and the identification of its peak timing at each study area (Table A1).

https://doi.org/10.5194/egusphere-2025-6409
Preprint. Discussion started: 12 January 2026

The height of the water flow in a given area is an important asset for estimating the extent of flooding, especially when considering the typical topography of a river and its floodplain. However, river gauges are not widespread in Central Chile, so in some cases, we had to use data from gauges located several kilometers upstream, near the headwaters (Figure 2).

We extracted datasets from the Dirección General de Aguas (DGA) for seven river gauges (labeled A to E in Figure 2). Most of these datasets were incomplete, possibly due to the flooding events themselves. To create a complete time series for each gauge, we aggregated the high temporal resolution data (hourly) into daily averages and standard deviations.

2.2.2 Historical water occurrence assessment

Historical water presence was quantified using the Global Surface Water (GSW) 1.4 dataset (Pekel et al., 2016). This dataset allowed us to determine the percentage of time each pixel in the study areas was historically classified as water between 1984 and 2021. To statistically characterize the frequency distribution of water occurrence within each site, we fitted a log-normal distribution to the histogram of the water occurrence pixel population. The mode and standard deviation derived from this fitting were used to understand the typical hydrological variability of the floodplains.

2.2.3 SAR processing, filtering, and flood index optimization

Sentinel-1 imagery, acquired in both ascending and descending orbits (where available) and pre-processed in GEE for thermal noise removal, radiometric calibration, and terrain correction, was utilized. The resultant σ_0 backscattering coefficients were subjected to two geospatial filters designed to enhance the signal-to-noise ratio and refine the initial flood masks (Figure 3).

First, a topographical filter derived from the Copernicus DEM was applied, excluding all pixels with a slope greater than 5 degrees. This value is consistent with common practice in flood mapping studies and was found to provide the optimal fit in mitigating layover and shadowing effects in the high-relief areas of the study region. Second, a filter based on the GSW database was used to mask out permanent water bodies. Pixels with a historical water occurrence greater than 10% were excluded. This threshold was selected as the most effective pragmatic balance during our initial calibration to delineate ephemeral flood zones from historically persistent water bodies. A 10% occurrence mask ensures that the change detection is focused strictly on transient, event-driven inundation outside the typical, low-variability river channel and its immediate, long-term fringe within the Mataquito and Maule floodplains.

The final flood extent mapping was conducted by applying three established SAR-based flood indices to the filtered imagery: the Difference Image Index (DII, Eq. 1), the Ratio Index (RI, Eq. 2), and the Normalized Difference Flood Index (NDFI, Eq. 3) (Hamidi et al., 2023). These indices, which utilize the σ_0 backscattering from the reference date ($\sigma_{0_{reference}}$) and the flood date ($\sigma_{0_{flood}}$).

The reference image ($\sigma_{0_{reference}}$) was consistently selected as the nearest available Sentinel-1 image acquired during the preceding dry season (June–July 2019), ensuring minimal water presence to establish a reliable baseline backscatter.

$$DII = |min(\sigma_{0_{flood}})| - |mean(\sigma_{0_{reference}})| \quad (1)$$

https://doi.org/10.5194/egusphere-2025-6409
Preprint. Discussion started: 12 January 2026

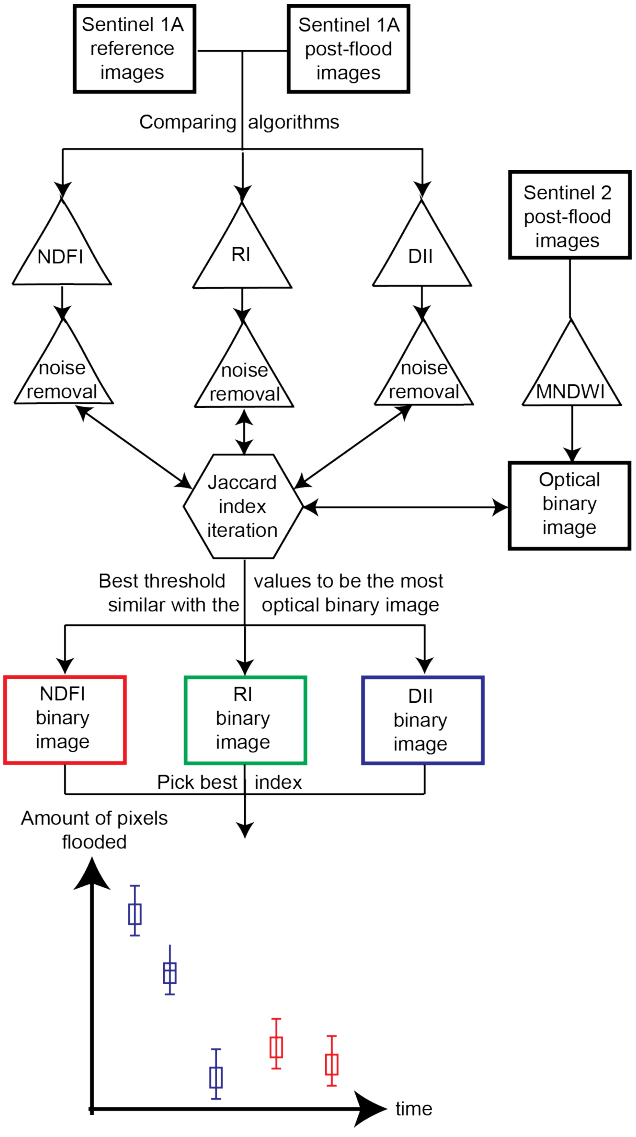

Figure 3. Workflow for identifying flooded areas using satellite imagery. The process involves comparing multiple indices—the Normalized Difference Flooding Index (NDFI), Ratio Index (RI), and Difference Image Index (DII)—against a ground-truth reference derived from the Modified Normalized Difference Water Index (MNDWI). The best-performing index is determined using an iterative Jaccard index calculation, based on the methodology by Hamidi et al. (2023)

.

$$RI = \frac{|min(\sigma_{0_{flood}})|}{|mean(\sigma_{0_{reference}})|} \tag{2}$$

https://doi.org/10.5194/egusphere-2025-6409
Preprint. Discussion started: 12 January 2026

$$NDFI = \frac{|mean(\sigma_{0_{reference}})| - |min(\sigma_{0_{flood}})|}{|mean(\sigma_{0_{reference}})| + |min(\sigma_{0_{flood}})|} \tag{3}$$

The variables in these indices follow the conventions established by Hamidi et al. (2023). Specifically, $|mean(\sigma_{0_{\text{reference}}})|$ represents the mean σ_0 value across the entire reference image raster, and $|min(\sigma_{0_{\text{flood}}})|$ is the σ_0 value of the individual flood-date pixel being tested, thereby identifying pixels where backscatter drops significantly below the established baseline.

The optimal threshold value for each index was determined via the iterative optimization of the K-factor (Eq. 4). Following the validation methodology of Hamidi et al. (2023), this process adjusts the K-factor to derive the threshold that maximizes the Jaccard Index against a near-concurrent optical ground-truth: the Modified Normalized Difference Water Index (MNDWI) (Eq. 5), derived from Sentinel-2 imagery (Hui et al., 2008). The methodology ensures the selection of the threshold that provides the maximum statistical agreement between the SAR-derived extent and the optical reference (Figure 3).

$$Best\ Threshold_{Index} = Mean_{Index} \pm (K \times Std_{Index}) \tag{4}$$

$$MNDWI = \frac{GREEN - SWIR}{GREEN + SWIR} \tag{5}$$

3 Results

3.1 Hydrograph response and event characteristics

Rainfall analysis, derived from aggregated GPM IMERG data over the studied catchments (Section 2.2.1), confirmed that the August 2023 event exhibited significantly higher accumulated intensity compared to the June event (Figure 4). This difference in forcing is reflected across the monitored sites (Figure 4a–e).

The river gauge time series obtained from the DGA network exhibits a flash-flood hydrological response. During the June event, the Canal de evacuación C. Pehuenche gauge (labeled 'Colbún' in Figure 4a) - the only station with a complete flood record - demonstrated an extremely rapid recession: the river height decreased from its peak near 4 meters to approximately half that height within just two days. The August event exhibited a similarly rapid recession, peaking near the instrument's reading limit before receding rapidly, dropping to just over 2 meters (approximately a 50% reduction from the peak) within four days (Figure 4a).

This rapid recession was even more pronounced at sites further north. For instance, the Río Claro en los Queñes gauge (labeled 'Teno' in Figure 4e) recorded a peak height of almost 4 meters. Yet, the river returned to near-baseflow conditions (below 2 meters) faster than the sites in the Maule watershed (Colbún and San Javier). These observations confirm that the floodwaters did not persist in the floodplains for long periods. Note that several gauges, including Estero Upeo en Upeo gauge (labeled 'Lontué' in Figure 4c) and Río Mataquito en Licantén gauge (labeled 'Hualañé' in Figure 4d), show data gaps during the peak of the events, which limit the exact quantification of maximum discharge.

https://doi.org/10.5194/egusphere-2025-6409
Preprint. Discussion started: 12 January 2026

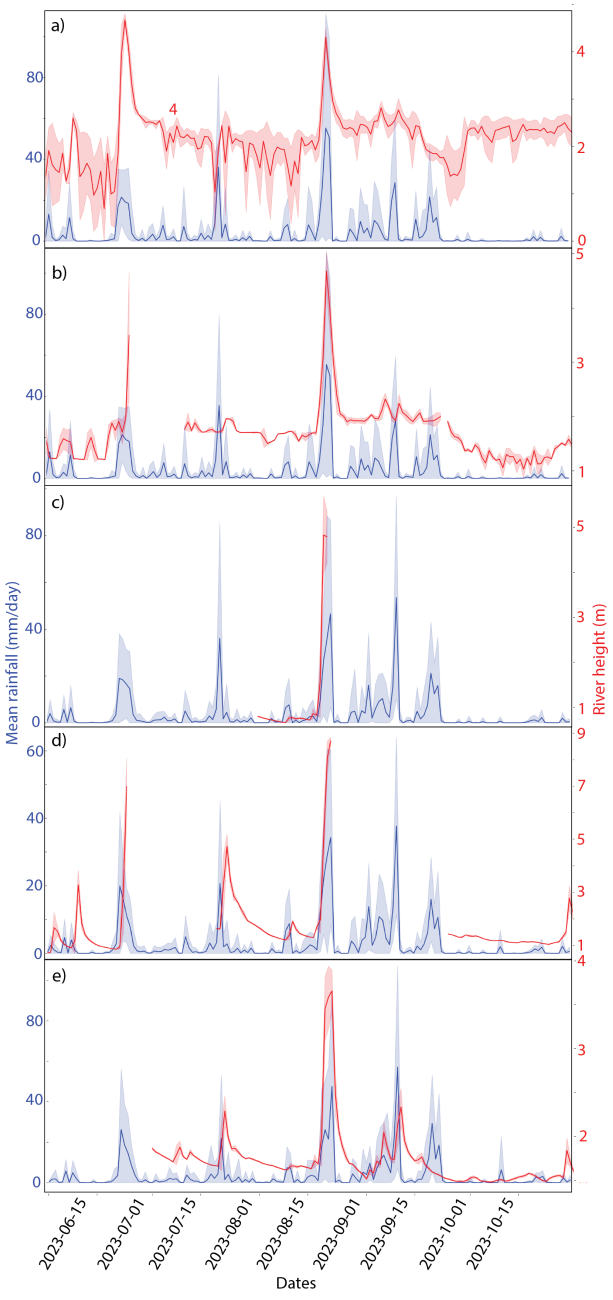

Figure 4. Time series analysis of the two extreme hydrometeorological events: daily averaged rainfall (GPM IMERG, blue) and river height evolution (DGA gauges, red). The data illustrate the flash-flood response, characterized by rapid peak and subsequent fast recession rates, across the five study areas: (a) Colbún, (b) San Javier, (c) Lontué, (d) Hualañé, and (e) Teno.

https://doi.org/10.5194/egusphere-2025-6409
Preprint. Discussion started: 12 January 2026

3.2 Historical water occurrence

The analyzed areas exhibit diverse water occurrence histories due to their distinct catchments and varying environmental pressures. For instance, the Colbún area has the lowest water occurrence, with a peak of only 3% of pixels classified as water (Figure 5a). In contrast, San Javier, located in the same watershed just a few kilometers to the west, shows a significantly higher peak of 16% (Figure 5b).

In the Mataquito watershed, the Lontué area has a water occurrence peak of 13% with a standard deviation of 18% (Figure 5c). Hualañé, also within the same watershed, shows a similar peak of 14% but a much higher standard deviation of 34% (Figure 5d). Further north, the Teno area presents values comparable to Lontué, with a 14% peak and a standard deviation of 19% (Figure 5e).

3.3 Index calibration performance

A primary finding is that images acquired on the same day but from different orbits (ascending or descending) often exhibit different threshold index values and Jaccard index scores when compared to the same optical ground-truth images (Figure 6). Overall, the Difference Image Index (DII) showed the highest correlation with the optical binary image (75%), followed by the Ratio Index (RI) (20%) and the Normalized Difference Flood Index (NDFI) (5%).

The highest Jaccard scores were consistently observed within the Maule Watershed (Colbún and San Javier), suggesting better statistical agreement between SAR and the optical ground truth in these sites. Conversely, the lowest scores were recorded in the Mataquito Watershed (Lontué and Hualañé) and the Teno area, with Lontué exhibiting the absolute minimum score (0.3).

Across all indices, there was a higher level of agreement between the optical and Sentinel-1 images for the first flood event (red-dashed lines in Figure 5), with a notable exception in the Hualañé area (Figure 6d). We note that the lower agreement in the Hualañé area coincides with a known data limitation during the reference period, specifically the absence of Sentinel-1A data. This incomplete baseline likely contributed to the reduced correlation observed for this site.

3.4 Flood extent evolution

Analysis of the optimal flood maps reveals distinct spatial variations in the maximum mapped flood extent between the two events (Figure 7). In the Colbún, Hualañé, and Teno sites, the maximum inundation area estimated during the June (first) event was demonstrably larger than the extent mapped during the subsequent August (second) event. Conversely, the flood extent estimations for San Javier and Lontué showed similar maximal areas across both events. Crucially, across all five sites, the mapped flood extent never fully inundated the entire defined floodplain area at the precise moment of satellite acquisition.

The temporal analysis of mapped flood extent demonstrates a strong correlation between the maximum detected flood area and the timing of the Sentinel-1 acquisition relative to the precipitation peak (Figure 8). The largest flood extensions were consistently mapped when the satellite overpass coincided closely with the peak precipitation date (e.g., Colbún and Teno during the June event, Figure 8a, e). Conversely, the generally smaller flood extents observed during the August event can be directly linked to the larger time gap between the peak rainfall and the first available SAR acquisition date. This trend directly

https://doi.org/10.5194/egusphere-2025-6409
Preprint. Discussion started: 12 January 2026

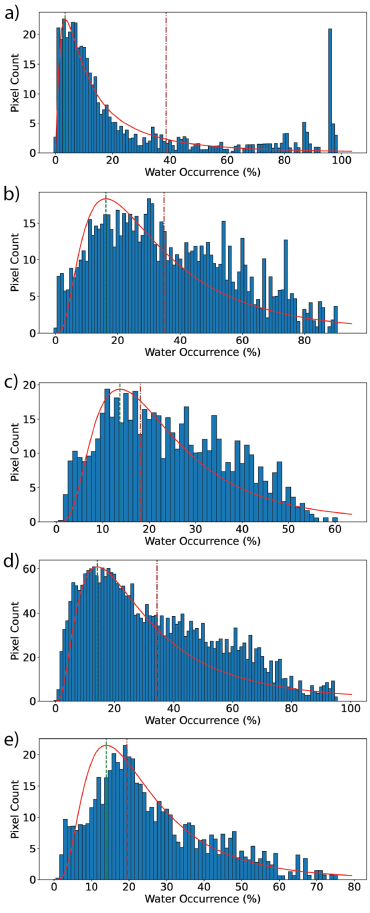

Figure 5. Histograms of historical water occurrence for the five specific study areas (see Figure 2), derived from the GSW 1.4 dataset from 1984 to 2021 (Pekel et al., 2016). The data were fitted to a log-normal distribution, where the dashed green line indicates the mode value and the dashed red line represents the standard deviation for each plot. Plots correspond to: (a) Colbún, (b) San Javier, (c) Lontué, (d) Hualañé, and (e) Teno.

confirms the rapid recession rate observed in the DGA hydrographs (Section 3.1), demonstrating that a delay of even 24–48 hours in SAR acquisition significantly reduces the estimated flood extent and leads to a severe underestimation of the maximum inundation area.

https://doi.org/10.5194/egusphere-2025-6409
Preprint. Discussion started: 12 January 2026

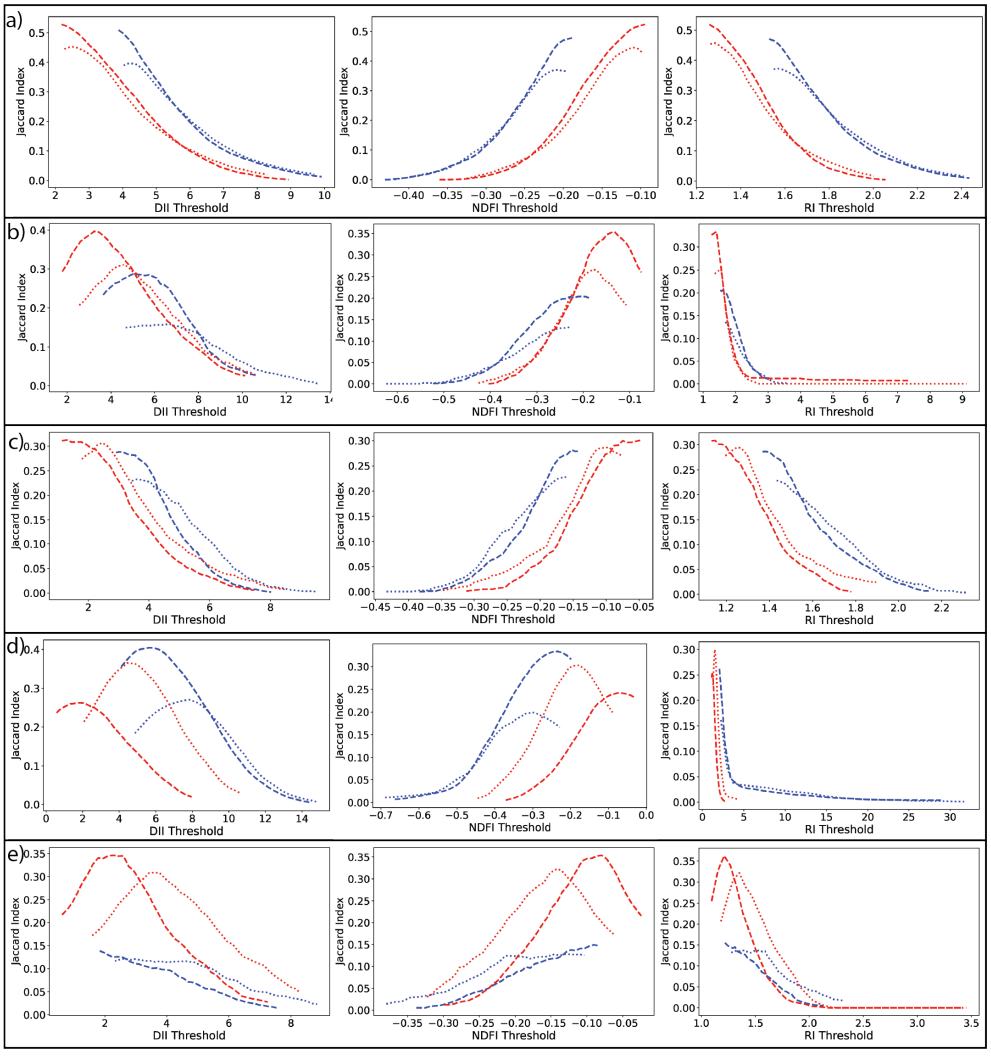

Figure 6. Quantitative estimation of the best threshold value per index per orbit per flood event. In blue are displayed the calculations for all Sentinel 1 Ascending orbits, meanwhile in red are all the descending orbits. In addition, the dashed lines corresponds to all the first flood event (June), meanwhile the dotted lines corresponds to the second event (August). The plots correspond to: a) Colbún, b) San Javier, c) Lontué, d) Hualañé, and e) Teno.

https://doi.org/10.5194/egusphere-2025-6409
Preprint. Discussion started: 12 January 2026

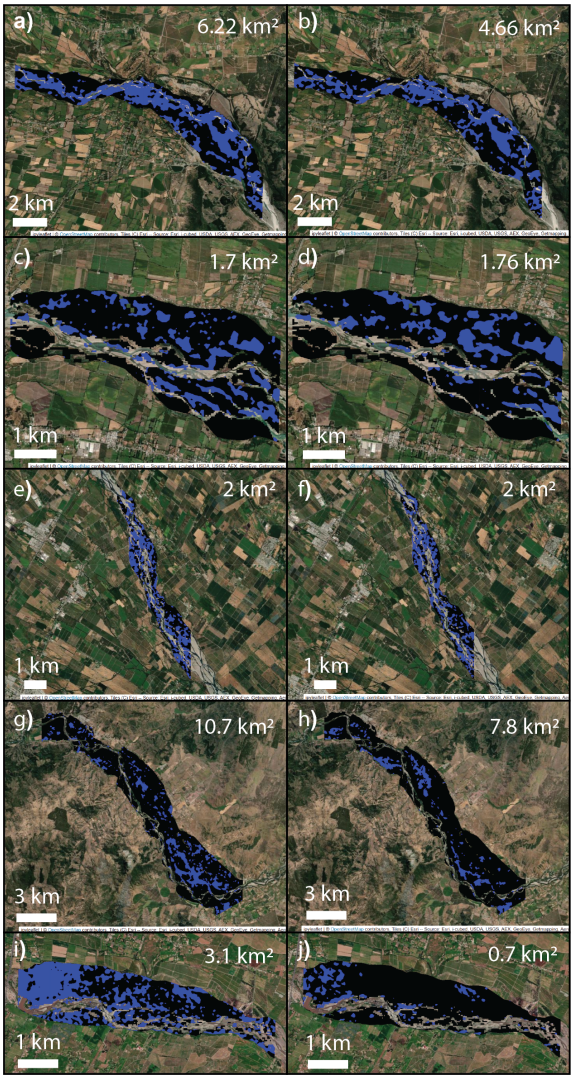

Figure 7. The figure displays the optimal flood maps for each study area and rainfall event. These maps were generated using the Sentinel-1 index that achieved the highest Jaccard index score when compared to the Sentinel-2 ground-truth imagery. The specific index and track used for each map were: a) Colbún (first event): DII from the ascending track; b) Colbún (second event): DII from the ascending track; c) San Javier (first event): DII from the ascending track; d) San Javier (second event): DII from the ascending track; e) Lontué (first event): DII from the ascending track; f) Lontué (second event): DII from the ascending track; g) Hualañé (first event): DII from the descending track; h) Hualañé (second event): DII from the ascending track; i) Teno (first event): RI from the ascending track; and j) Teno (second event): RI from the ascending track.

https://doi.org/10.5194/egusphere-2025-6409
Preprint. Discussion started: 12 January 2026

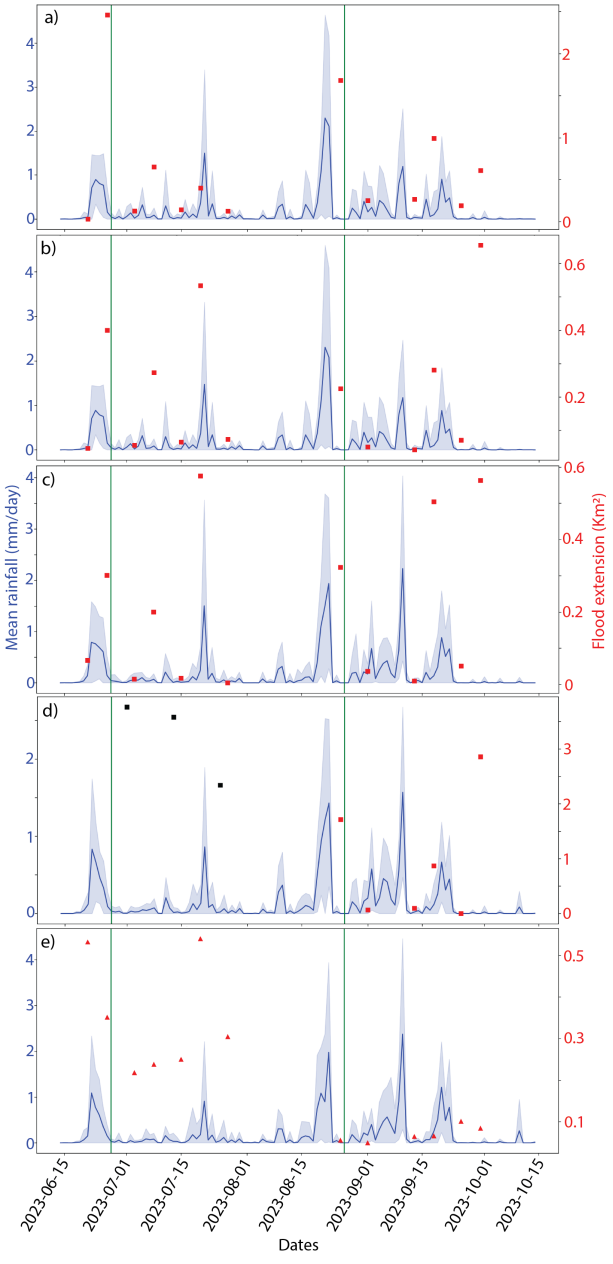

Figure 8. Time series of flood extension using the best index for each location, orbital path and rain event. a) Colbún, b) San Javier, c) Lontué, d) Hualañé, and e) Teno. In red, the descending path, and blue is ascending path. The rectangles corresponds to DII measurements while triangles are RI measurements.

https://doi.org/10.5194/egusphere-2025-6409
Preprint. Discussion started: 12 January 2026

4 Discussion

4.1 The critical role of image timing

Past research has already pointed out that the accurate identification of flooded areas must account for the satellite acquisition date relative to the peak of the rainfall event (e.g., Tanim et al., 2022). Building on this understanding, our primary objective was to critically quantify the uncertainty in flood extent estimation introduced by satellite acquisition timing relative to the peak of the hydrometeorological event. Our results conclusively demonstrate that estimating the maximum flood extent in these Central Chilean river systems is fundamentally limited by the timing of the Sentinel-1 overpass.

This limitation is a direct consequence of the flash-flood hydrological regime characteristic of the Andean-influenced Mataquito and Maule watersheds, a finding strongly supported by the DGA gauge analysis (Section 3.1). This rapid response is consistent with observations in neighboring catchments, such as the Biobío watershed that affected Concepción (Rojas et al., 2017). The observed extremely rapid recession rate, where river height can drop by approximately 50% within just four days of the peak, means that floodwaters do not persist long enough in the floodplains to guarantee consistent satellite capture during peak inundation. Furthermore, this rapid draining process often leaves behind residual surface water bodies (ponds) on the floodplain. Since our ground-truth optical images (MNDWI) were also acquired at a non-peak time, this residual water complicates the statistical comparison, potentially reducing the statistical agreement (Jaccard scores) between the SAR-derived and optical masks.

The temporal analysis shown in Figure 8 provides compelling evidence for this phenomenon. We observed that the largest flood extents were consistently mapped during the June event, where the optimized SAR image acquisition occurred in close temporal proximity to the rainfall peak. Conversely, the significantly smaller extents mapped during the August event, despite the higher rainfall intensity, are directly attributable to the larger time gap between the rainfall peak and the first available Sentinel-1 image. This disparity confirms that even a delay of 24 - 48 hours in acquisition can result in a severe underestimation of the true maximum flood footprint, which has serious implications for accurate risk assessment.

This finding carries significant implications for operational flood mapping in rapidly responding basins. Since the maximum extent of the flooding is transient, relying solely on Sentinel-1's 6-day repeat cycle is insufficient for capturing the event's true peak impact. To address this, we argue that future flood risk assessments in high-relief environments must integrate SAR-based flood extents with hydraulic modeling or high-frequency aerial surveys to accurately interpolate the maximum extent that occurred at the unobserved peak discharge (Chlumsky et al., 2025).

4.2 Methodological Considerations and Challenges

The statistical performance of the iterative index optimization framework revealed that the methodology, while rigorous, faced significant challenges when applied to the high-relief, rapidly responding catchments of Central Chile. This difficulty is quantified by the generally low Jaccard Index scores, which peaked at approximately 0.6 (Section 3.3). This moderate level of statistical agreement stems from several inherent physical and temporal constraints:

https://doi.org/10.5194/egusphere-2025-6409
Preprint. Discussion started: 12 January 2026

1. Topographical Complexity and Filtering: The Maule and Mataquito watersheds present a high degree of geomorphological complexity. Although we applied a conservative $\mathbf{5}^{\circ}$ slope filter (Section 2.2.3) to exclude areas prone to SAR artifacts (layover and shadowing), this filtering process itself necessarily reduces the spatial extent available for validation. Furthermore, the low Jaccard scores in areas like Lontué (as low as 0.3) are likely related to persistent localized topographical effects that remain in the floodplain, such as complex micro-relief, which generate backscattering ambiguities that cannot be resolved by the generalized index approach.

2. Geological and Hydrogeological Control: The geological heterogeneities of the landscape likely exert a strong hydrogeological control on water retention. Specifically, the extensive gravel deposits typical of the Central Depression enhance permeability and rapid infiltration, while the narrower, confined channels and fine-grained floodplain deposits prevalent in the Coastal Cordillera influence flow velocity and local storage. These differences in geological makeup and channel geometry significantly affect the rate of infiltration and subsurface drainage, thereby limiting the duration that floodwater remains visible for satellite capture.

3. Impact of Temporal Mismatch: The Jaccard optimization requires comparison against a concurrent optical ground-truth (MNDWI). The high recession rate of the river means that the optical reference image (even if taken close to the SAR image) captured the flood extent at a slightly different stage of recession. This temporal mismatch results in inevitable spatial disagreement between the two binary masks, preventing the Jaccard Index from achieving the higher scores (e.g., > 0.8) often reported in studies of large, slow-moving floodplains. The residual ponding effect further exacerbates this discord, as temporary ponds detected by the SAR image may have drained by the time the optical image was acquired, and vice versa.

Despite the low overall statistical agreement, the framework successfully identified the Difference Image Index (DII) as the superior performer, consistently achieving the highest Jaccard scores in 75% of the tested acquisitions (Section 3.3). The DII's robustness in this environment is attributed to its direct reliance on the absolute magnitude of change between the reference and flood image, making it less susceptible to noise and small variations in backscatter compared to ratio-based indices like the RI or NDFI, particularly in complex terrain. In summary, while the method proposed by Hamidi et al. (2023) effectively finds the most statistically optimal threshold (K-factor) achievable for a given SAR-optical pair, our application demonstrates that the true limitation is not the calibration method itself, but the underlying physical constraints of rapid hydrological recession and complex topography in high-relief environments.

4.3 Implications for stakeholders and flood risk assessment

Our findings present two critical implications for stakeholders and water resource managers. First, the uncertainty introduced by the rapid recession rate fundamentally limits the utility of retrospective SAR analysis for capturing maximum event severity. Current operational flood maps based on Sentinel-1, particularly those created shortly after a peak event, likely represent a minimum flood extent, potentially leading to the underestimation of affected infrastructure and required disaster relief funds. The reliance on models or high-frequency data for peak interpolation (as argued in Section 4.1) is therefore not merely a

https://doi.org/10.5194/egusphere-2025-6409
Preprint. Discussion started: 12 January 2026

technical refinement, but an essential requirement for robust hazard planning. Second, the comparison between historical water occurrence and event-based inundation yields a crucial insight for land-use planning. The Colbún study area serves as a key example: Figure 5a shows a near-absence of permanent water (peak $\sim 3\%$), yet Figures 7a and 7b confirm that this area experienced significant flooding during both 2023 events. This discrepancy is a strong warning that the absence of permanent water bodies (low historical water occurrence) does not guarantee immunity from inundation during extreme precipitation events. Land-use planning and infrastructure development cannot rely solely on historical data that filters out transient floodplains. Stakeholders must consider areas with low historical water presence but high hydrological vulnerability as primary flood risk zones. This is particularly relevant in areas experiencing shifts towards intensified precipitation events due to climate change.

5 Conclusions

This study provided critical quantitative evidence regarding the challenges of using Sentinel-1 SAR data for flood extent mapping in the high-relief, flash-flood-prone river systems of Central Chile. We conclusively demonstrate that the accurate estimation of maximum flood extent is fundamentally limited by the timing of the satellite acquisition relative to the hydrological event peak. This limitation stems directly from the flash-flood hydrological regime of the Mataquito and Maule watersheds, characterized by an extremely rapid recession rate with river height dropping approximately 50% within four days of the peak. This quick drainage means the maximum flood footprint is ta and often missed by the satellite's return cycle, resulting in a severe underestimation of the true event impact.

Our methodological contribution successfully applied and validated the iterative Jaccard optimization framework, identifying the Difference Image Index (DII) as the most robust indicator (75% of optimal selections). However, the resulting Jaccard scores remained consistently low (<0.6). We conclude that this statistical performance is constrained not by the calibration method, but by physical limitations: the combined effects of complex topography, the rapid temporal mismatch between SAR and optical acquisitions, and residual ponding on the floodplain.

Ultimately, relying solely on the Sentinel-1 revisit cycle is insufficient for operational flood risk assessment in high-relief environments. To overcome this fundamental uncertainty and accurately capture the event's true peak, we strongly recommend that future assessments must integrate SAR-based monitoring with hydraulic modeling or high-frequency aerial surveys to interpolate the maximum flood extent that occurred during the unobserved peak discharge.

https://doi.org/10.5194/egusphere-2025-6409
Preprint. Discussion started: 12 January 2026

Appendix A: Relevant dataset

Table A1: Type of sensor, orbit and date of the first scene after each rain event per area.

Study area	Date of the peak of rain event	Sensor	Orbit	Date of flood detected
Colbún	24-06-2023 (first)	Sentinel 1	Ascending	26-06-2023
			Descending	26-06-2023
		Sentinel 2	Does not apply	27-06-2023
	21-08-2023 (second)	Sentinel 1	Ascending	25-08-2023
			Descending	25-08-2023
		Sentinel 2	Does not apply	26-08-2023
San Javier	24-06-2023 (first)	Sentinel 1	Ascending	26-06-2023
			Descending	26-06-2023
		Sentinel 2	Does not apply	27-06-2023
	21-08-2023 (second)	Sentinel 1	Ascending	25-08-2023
			Descending	25-08-2023
		Sentinel 2	Does not apply	26-08-2023
Hualañé	22-06-2023 (first)	Sentinel 1	Ascending	26-06-2023
			Descending	01-07-2023
		Sentinel 2	Does not apply	27-06-2023
	22-08-2023 (second)	Sentinel 1	Ascending	25-08-2023
			Descending	30-08-2023
		Sentinel 2	Does not apply	26-08-2023
Lontué	24-06-2023 (first)	Sentinel 1	Ascending	26-06-2023
			Descending	26-06-2023
		Sentinel 2	Does not apply	27-06-2023
	22-08-2023 (second)	Sentinel 1	Ascending	25-08-2023
			Descending	25-08-2023

https://doi.org/10.5194/egusphere-2025-6409
Preprint. Discussion started: 12 January 2026

Table A1 Type of sensor, orbit and date of the first scene after each rain event per area.

Study area	Date of the peak of rain event	Sensor	Orbit	Date of flood detected
		Sentinel 2	Does not apply	26-08-2023
Teno	22-06-2023 (first)	Sentinel 1	Ascending	21-06-2023
			Descending	26-06-2023
		Sentinel 2	Does not apply	27-06-2023
	22-08-2023 (second)	Sentinel 1	Ascending	25-08-2023
			Descending	25-08-2023
		Sentinel 2	Does not apply	26-08-2023

. We will provide the entire code and datasets used on Github repository written in both English and Spanish.

. LO designed the study, wrote the manuscript, and prepared and analyzed the data. GG participated in manuscript writing and editing, and data interpretation.

. The authors declare that they do not have any competing interests.

. We thank the FONDAP-ANID grant 1523A009, which funded the postdoctoral fellowship of LO and the research activities.

https://doi.org/10.5194/egusphere-2025-6409
Preprint. Discussion started: 12 January 2026

References

Acharya, T. D., Subedi, A., and Lee, D. H.: Evaluation of Water Indices for Surface Water Extraction in a Landsat 8 Scene of Nepal, Sensors, 18, https://doi.org/10.3390/s18082580, 2018.

Chlumsky, R., Craig, J. R., and Tolson, B. A.: A reach-integrated hydraulic modelling approach for large-scale and real-time inundation mapping, Geoscientific Model Development, 18, 3387–3403, https://doi.org/10.5194/gmd-18-3387-2025, 2025.

CIGIDEN: Informe Post Desastre, Evento: Inundaciones 21 - 26 junio. Cuencas del Río Mataquito y Río Maule (Región del Maule), Tech. rep., Análisis Satelital: Olivares, L., González, G., Matabenítez, G., CIGIDEN, Santiago, Chile, 2023.

European Space Agency, E.: Copernicus Global Digital Elevation Model., Tech. rep., Distributed by OpenTopography., https://doi.org/https://doi.org/10.5069/G9028PQB, 2024.

Feyisa, G. L., Meilby, H., Fensholt, R., and Proud, S. R.: Automated Water Extraction Index: A new technique for surface water mapping using Landsat imagery, Remote Sensing of Environment, 140, 23–35, https://doi.org/https://doi.org/10.1016/j.rse.2013.08.029, 2014.

Fisher, A., Flood, N., and Danaher, T.: Comparing Landsat water index methods for automated water classification in eastern Australia, Remote Sensing of Environment, 175, 167–182, https://doi.org/https://doi.org/10.1016/j.rse.2015.12.055, 2016.

Gao, B.-c.: NDWI—A normalized difference water index for remote sensing of vegetation liquid water from space, Remote Sensing of Environment, 58, 257–266, https://doi.org/https://doi.org/10.1016/S0034-4257(96)00067-3, 1996.

Hamidi, E., Peter, B. G., Muñoz, D. F., Moftakhari, H., and Moradkhani, H.: Fast Flood Extent Monitoring With SAR Change Detection Using Google Earth Engine, IEEE Transactions on Geoscience and Remote Sensing, 61, 1–19, https://doi.org/10.1109/TGRS.2023.3240097, 2023.

Huang, C., Chen, Y., Zhang, S., and Wu, J.: Detecting, Extracting, and Monitoring Surface Water From Space Using Optical Sensors: A Review, Reviews of Geophysics, 56, 333–360, https://doi.org/https://doi.org/10.1029/2018RG000598, 2018.

Huffman, G. Stocker, E. B. D., Nelkin, E., and Tan, J.: GPM IMERG Final Precipitation L3 1 month 0.1 degree x 0.1 degree V06, Greenbelt, MD, Tech. rep., Goddard Earth Sciences Data and Information Services Center (GES DISC), https://doi.org/10.5067/GPM/IMERG/3B-MONTH/06, 2019.

Hui, F., Xu, B., Huang, H., Yu, Q., and and, P. G.: Modelling spatial-temporal change of Poyang Lake using multitemporal Landsat imagery, International Journal of Remote Sensing, 29, 5767–5784, https://doi.org/10.1080/01431160802060912, 2008.

Liang, J. and Liu, D.: A local thresholding approach to flood water delineation using Sentinel-1 SAR imagery, ISPRS Journal of Photogrammetry and Remote Sensing, 159, 53–62, https://doi.org/https://doi.org/10.1016/j.isprsjprs.2019.10.017, 2020.

Moharrami, M., Javanbakht, M., and Attarchi, S.: Automatic flood detection using sentinel-1 images on the google earth engine, Environmental Monitoring and Assessment, 193, 248, https://doi.org/10.1007/s10661-021-09037-7, 2021.

Pekel, J.-F., Cottam, A., Gorelick, N., and Belward, A. S.: High-resolution mapping of global surface water and its long-term changes, Nature, 540, 418–422, https://doi.org/10.1038/nature20584, 2016.

Rojas, O., Mardones, M., Rojas, C., Martínez, C., and Flores, L.: Urban Growth and Flood Disasters in the Coastal River Basin of South-Central Chile (1943–2011), Sustainability, 9, https://doi.org/10.3390/su9020195, 2017.

Tanim, A. H., McRae, C. B., Tavakol-Davani, H., and Goharian, E.: Flood Detection in Urban Areas Using Satellite Imagery and Machine Learning, Water, 14, https://doi.org/10.3390/w14071140, 2022.

Tauqeer, A., Stephen, H., and Ahmad, S.: Flood Extent Mapping of the 2022 Sindh Flood: A Remote Sensing Analysis Using SAR, Optical Data, and Google Engine Platform, pp. 406–421, https://doi.org/10.1061/9780784486184.037, 2025.

https://doi.org/10.5194/egusphere-2025-6409
Preprint. Discussion started: 12 January 2026

Tripathy, P., M. T.: Global Flood Mapper: a novel Google Earth Engine application for rapid flood mapping using Sentinel-1 SAR., Natural Hazards, 114, https://doi.org/10.1007/s11069-022-05428-2, 2022.

Twele, A., Cao, W., Plank, S., and Martinis, S.: Sentinel-1-based flood mapping: a fully automated processing chain, International Journal of Remote Sensing, 37, 2990–3004, https://doi.org/10.1080/01431161.2016.1192304, 2016.